RSC Advances

ROYAL SOCIETY OF CHEMISTRY

www.rsc.org/advances

Scalable preparation of silicon@graphite/carbon microspheres as high-performance lithium-ion battery anode materials

Hao Wang,[a] Jian Xie,[a,b] Shichao Zhang,[c] Gaoshao Cao[a,b*] and Xinbing Zhao[a,b]

[a] *State Key Laboratory of Silicon Materials, School of Materials Science and Engineering, Zhejiang University, Hangzhou 310027, P. R. China*
[b] *Key Laboratory of Advanced Materials and Applications for Batteries of Zhejiang Province, Hangzhou 310027, P. R. China. E-mail: gscao@zju.edu.cn; Fax: +86-571-87951451; Tel: +86-571-87951451*
[c] *School of Materials Science and Engineering, Beijing University of Aeronautics and Astronautics, Beijing 100191, P. R. China*

† Electronic supplementary information (ESI) available: XRD and Raman spectra of amorphous carbon, EIS plots of FG, Si@FG and Si@FG/C-1, cycling stability of the Si@FG/C-1, Si@FG, FG, amorphous carbon and Si, and SEM images of Si@FG/C-1 and Si@FG electrodes before and after cycling. See DOI:

ABSTRACT

Silicon materials have received extensive research interest due to high specific capacity of 3579 mAh g^{-1} and appropriate potential of approximately 0.4 V *vs.* Li/Li^+. However, silicon materials suffer from poor cycling stability due to the intrinsic large volume changes upon cycling. In this work, silicon@flake-graphite/amorphous-carbon (Si@FG/C) composites were prepared by a controllable, scalable method. The Si@FG/C composites exhibit a porous spherical shape composed of Si nanoparticles, flake-like graphite and amorphous carbon. The pores in porous Si@FG/C can buffer the volume changes of Si upon cycling. The amorphous carbon provides conducting effect for Si and fixes Si nanoparticles on the FG during cycling. This unique structure leads to structural stability of the electrode and thereby good cycling stability. A capacity retention of 90% can be achieved for Si@FG/C-1 over 300 cycles at 500 mA g^{-1}. The composites also exhibit good rate capability due to the porous structure and effective conductive networks constructed by FG and amorphous carbon. Among the samples, Si@FG/C-3 demonstrates the best rate capability, where a capacity of 200 mAh g^{-1} can be obtained at a current density as high as 5 A g^{-1}.

1. Introduction

Although lithium-ion batteries(LIBs) with high energy density, long cycle life and environmental friendliness have been widely used in electrical vehicles (EVs), power tools, and portable electronic devices, they cannot completely satisfy the demands of technological applications.[1–5] Graphite, the dominant anode material in commercial LIBs, has a low theoretical special capacity of 372 mAh g^{-1}.[6–8] In contrast, silicon has a high theoretical capacity of 3579 mAh g^{-1}, which is ten times larger than those of graphite anodes.[9–11] In addition, Si shows a moderate potential of around 0.4 V *vs.* Li/Li^+. However, Si anodes suffer from limited cycle life due to volume expansion and contraction during discharge and charge, which gives rise to particle fracture and pulverization. This results in the loss of physical contact of active materials with conductive agent and current collector and the destruction of the solid electrolyte interphase (SEI), leading to rapid capacity fade.[12–17] At the same time, Si anodes exhibit low electronic conductivity and lithium-ion diffusion rate, causing sluggish electrode kinetics and poor rate capability.[18–20]

Many strategies have been taken to solve these problems, such as using Si particles with different nanostructures,[21,22] or morphologies,[23,24] using Si-based alloys instead of elemental Si,[25,26] and coating Si particles with another component.[27–29] For instance, a carbon-silicon-carbon (C@Si@C) nanotube sandwich structure was fabricated by a modified hydrothermal method combined with a chemical vapor deposition (CVD) process.[30] The obtained C@Si@C nanotube arrays exhibited excellent electrochemical performance due to the unique double-carbon-layer structure which assists in the formation of stable SEI layer and provides a continuous electronic conductive pathway. Si pomegranates prepared by a micro-emulsion approach and a carbon coating step could deliver a superior cyclability (97% capacity retention after 1000 cycles) and a high columbic efficiency (99.9%), because the void spaces accommodated the volume expansion of the

Si and the carbon component functioned as conducting framework and an electrolyte blocking layer.[31] A Si@$FeSi_y$/SiO_x hybrid structure synthesized by ammonia-assisted ball-milling route exhibited good cycling stability and high-rate capability, due to the effective improvement of electronic conductivity and accommodation of volume changes upon cycling.[32] Although various Si-based materials have been successful in extending the cycle life and rate performance of Si, it is difficult to realize a scalable preparation for these reported methods as a result of high cost and complicated production process.[33] Therefore, development of Si anode materials based on low cost and scalable procedure is urgent.

Herein, we developed a controllable, scalable method to synthesize Si@flake-graphite/amorphous-carbon (Si@FG/C) microspheres employing a combined ball-milling and spray-drying method,[34–36] and the experimental procedure is schematically presented in Fig. 1. Commercial Si nanoparticles and flake-like graphite are sufficiently mixed by dry ball milling. Subsequently, spherical Si@FG/C was obtained with a spray-drying process followed by high-temperature heating, where glucose and polyvinylpyrrolidone (PVP) were used first as binder to combine Si and graphite flakes and then as carbon source to coat Si and graphite. The Si@FG/C porous microspheres exhibit superior electrochemical performance with a capacity over 400 mAh g^{-1} retained after 300 cycles, showing promising applications as high-performance anode materials for LIBs.

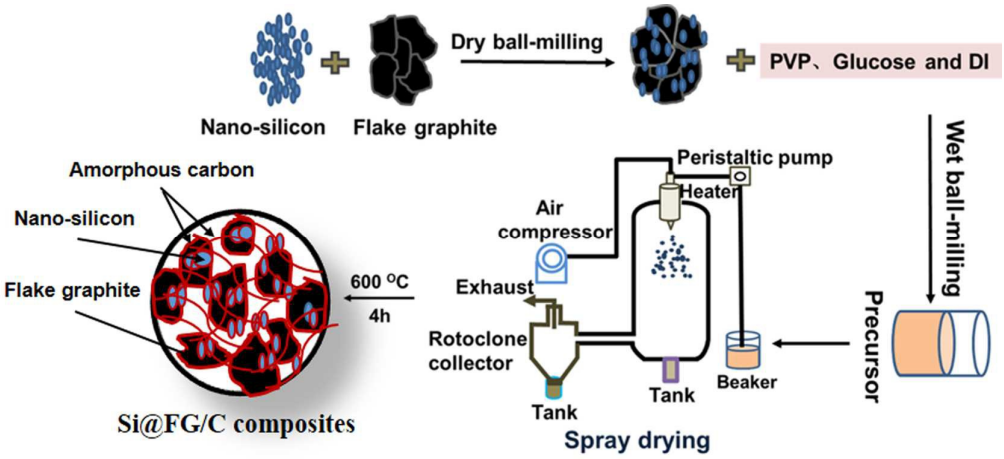

Fig.1. Illustration of the preparation process of Si@FG/C microspheres.

2. Experimental

2.1 Preparation of Si@FG/C microspheres

Commercial Si nanoparticles (average particle size 80 nm, 99.9% purity, Nanjing Emperor Nano Material Co., Ltd., China) and flake-like graphite (Qingdao Jinrilai Graphite Co., Ltd., China) (Si:graphite = 1:9, in weight) were first mixed by dry ball milling (ball-to-solid = 1:9, in weight) for 2 h at 220 rpm to obtain a Si@FG mixture. Then, the mixture was mixed with glucose and PVP in deionized water (Si@FG:glucose:PVP = 1.2:0.4:0.6, in weight) followed by wet ball milling for 2.8 h at 220 rpm. After that, the mixture was spray-dried using a spray-drying machine (YC-015, Shanghai Pilotech Instrument and Equipment Co., Ltd., China) with inlet temperature of 250 °C and outlet temperature of 110 °C. The precursor was collected, and placed in an Al_2O_3 boat which was loaded into a tubular furnace. After being purged with Ar, the furnace was heated to 600 °C at 5 °C min^{-1}, held for 4 h, and cooled to room temperature in Ar flow. The solid product was collected and grounded in the mortar. The obtained sample was named Si@FG/C-1. Another two samples with different Si contents were also prepared with a similar route by adjusting Si/graphite ratios (1:7 and 1:5, in weight) and were named Si@FG/C-2 and Si@FG/C-3), respectively. For comparison, amorphous carbon was also prepared by the carbonization of glucose at 600 and 1000 °C for 4 h under Ar flow.

2.2 Materials characterization

The phases of the materials were measured by X-ray diffraction (XRD) on a RigakuD/Max-2550pc powder diffractometer equipped with Cu K_α radiation (λ= 0.1542 nm). Thermogravimetric (TG) analysis was conducted on a DSCQ1000 instrument from 25 to 900 ºC at a heating rate of 10 ºC min^{-1} in air. Particle size distribution was measured using a laser particle size analyzer (Model LS-230 Coulter, Coulter Corporation, Ltd., America). Raman spectra were collected on a JOBIN-Yvon Labor Raman HR-800 Raman system using a 514.5 nm Ar-ion laser at 10 mW. Scanning electron microscopy (SEM) images were characterized with an S-4800 field-emission scanning electron microscope (Hitachi, Japan). Transmission electron microscopy (TEM) and high-resolution TEM (HRTEM) images were observed with FEI Tecnai G2 F20 S-TWIN high-resolution transmission electron microscope with an acceleration voltage of 200 KV.

2.3 Electrochemical measurements

Electrochemical performance of the Si@FG/C samples was evaluated by galvanostatic cycling using CR2025-type coin cells. The electrode slurry was made by dispersing 80 wt% Si@FG/C, 10 wt% acetylene black and 10 wt% polyacrylic acid (PAA) in N-methylpyrrolidone (NMP) with magnetic stirring for 2 h. Then, the slurry was coated uniformly on Cu foil and dried overnight at 80 °C under vacuum to yield the working electrodes. The active material loading was about 2.5 mg cm^{-2}. The electrodes were then assembled into half cells in an Ar-filled glove box using Li foil as the counter electrodes and Celgard 2300 membrane as the separators. The electrolyte used was 1 M $LiPF_6$ in ethylene carbonate (EC)/dimethyl carbonate (DMC) (1:1 in volume) with 5 vol% fluoroethylene carbonate (FEC). Galvanostatic charge/discharge testing was carried out at a voltage range of 0.01–1.5 V (*vs.* Li/Li^+) on a Neware BTS-5V-10mA battery cycler (Shenzhen, China). All the cells were cycled at 0.2 A g^{-1} for the first 5 cycles and then at 0.5 A g^{-1} for the later cycles. The current density and specific capacity were normalized to the total weight of the active materials. For

comparison, the electrochemical performance of Si nanoparticles, amorphous carbon and Si@FG were also investigated. Cyclic voltammetry (CV) measurements were performed on a Princeton Applied Research Versa-STAT3 electrochemistry workstation at 0.01–1.5 V (*vs.* Li/Li^+) with a scanning rate of 0.1 mV s^{-1}. Electrochemical impedance spectroscopy (EIS) measurements were carried on the electrochemistry workstation with an ac voltage of 5 mV amplitude in the frequency range from 10 mHz to 100 kHz. All electrochemical measurements were carried out at room temperature.

3. Results and discussion

Fig. 2a shows the SEM image of the as-received graphite. The graphite particles have a flake-like morphology with a smooth, dense surface and a particle size of 1–10 μm. The size distribution of graphite is appropriate to obtain spherical secondary particles after the spray drying and heat treatment processes. The pristine Si particles have a size of around 80 nm and tend to aggregate due to high surface energy of the nanoparticles (Fig. 2b). Thus, a ball-milling step is necessary to realize uniform dispersion of Si nanoparticles on FG. It can clearly be seen in Fig. 2c that the precursor exhibits a regular spherical morphology with a size range of 2–40 μm after spray drying. The enlarged view in Fig. 2d demonstrates that FG and Si particles are bond by glucose and PVP in a single microsphere. After being heated at 600 ºC for 4 h，the final product Si@FG/C-1can keep the spherical structure of the precursor (Fig. 2e). The magnified image of a single microsphere in Fig. 2f indicates that the surface of the microspheres exhibits a rough and porous morphology.

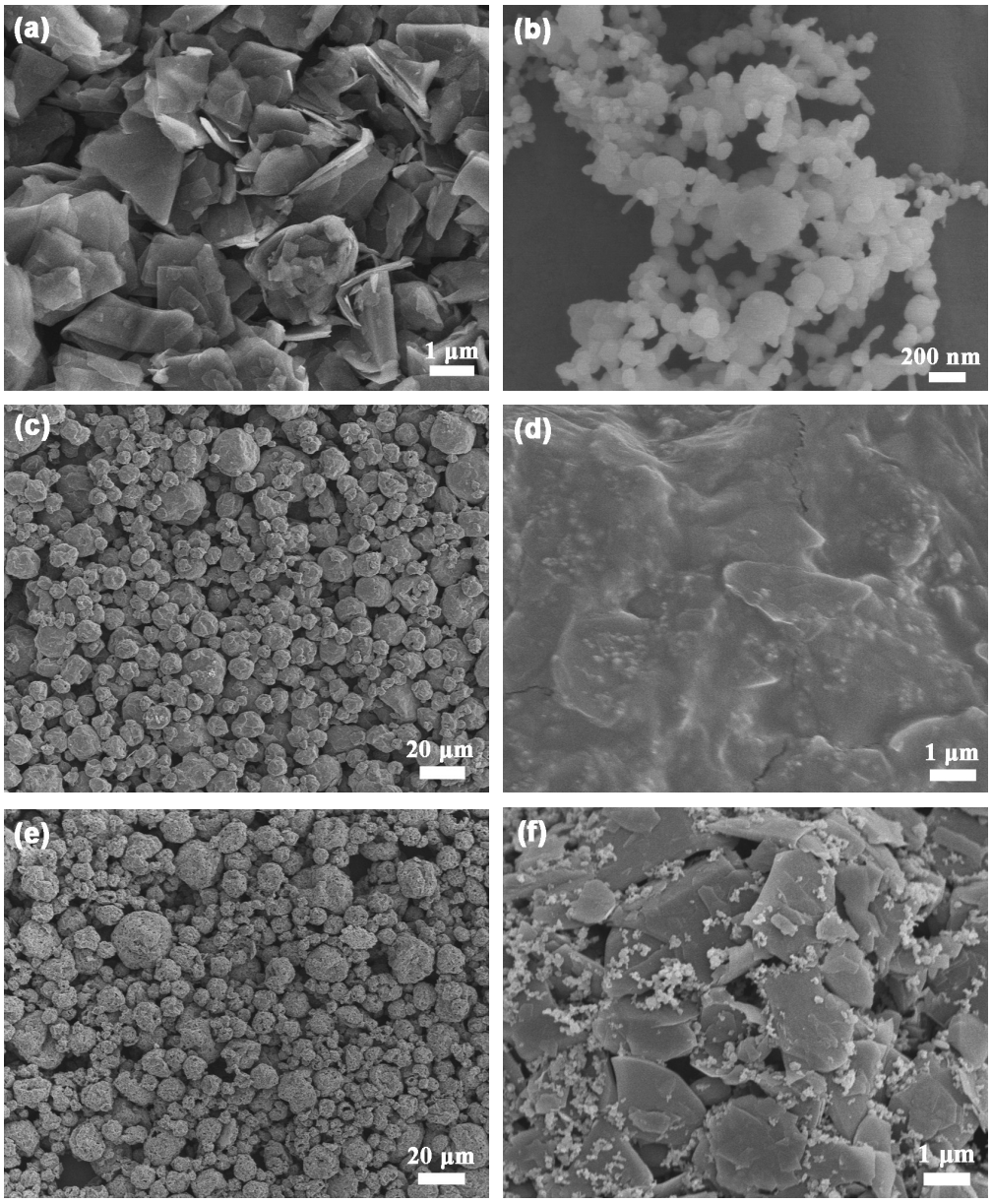

Fig. 2. SEM of (a) flake graphite, (b) silicon nanoparticles. (c) spray-dried precursor for Si@FG/C-1 microspheres, (d) enlarged view of (c), (e) Si@FG/C-1, and (f) enlarged view of (e).

The morphology and microstructure of Si@FG/C-1 microspheres were further characterized by TEM (Fig. 3a) and HRTEM (Fig. 3b). The lattice fringes with spacings of 0.31, 0.27 and 0.22 nm correspond to the (111) and (002) planes of Si and the (003) plane of FG, respectively. We can also observe irregular fringes in the image which suggests the formation of amorphous carbon from glucose and PVP. It can be seen that the thickness of the amorphous carbon layer is around 2.5 nm

for Si@FG/C-1. With the same preparation procedure and content of organic precursor, the other two samples have a similar thickness of the amorphous carbon layer. We try to increase or decrease the content of amorphous carbon in the composites. However it was found that the higher amorphous carbon content (thereby large thickness) would lead to good cycling stability but low initial coulombic efficiency and capacity. On the contrary, lower amorphous carbon content would lead to high initial coulombic efficiency and capacity but poor cycling stability. Therefore, the amorphous carbon content was optimized in our samples, which brings optimized capacity, initial coulombic efficiency and cycling stability as will discussed later. The presence of amorphous carbon not only provides the electronic conductivity for Si particles but also absorbs part of the strain arising from volume changes of Si particles.[37,38] In addition, the amorphous carbon can fix the Si nanoparticles on the surface of graphite flakes.

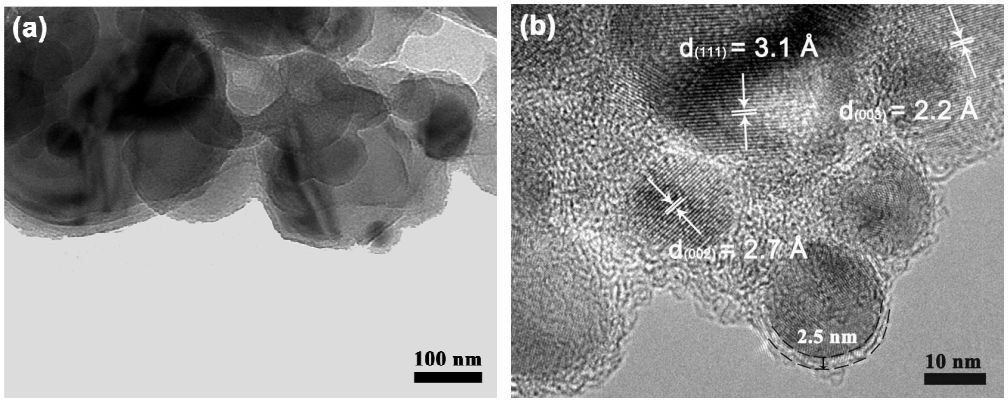

Fig.3. (a) TEM and (b) HRTEM images of the Si@FG/C-1.

As seen in Fig. 4a, for Si@FG/C and Si, there are five diffraction peaks at 2θ values of 28.4, 47.3, 56.1, 69.1 and 76.3, which can be assigned to (111), (220), (311), (400) and (331) planes of the Si (JCPDS no. 27–1402), respectively. Besides the Si phase, the observed peaks at 2θ values of 26.3, 42.2, 44.3, 50.4, 54.5 and 59.6 correspond to the (002), (100), (101), (102), (004) and (103) planes of graphitic carbon (JCPDS no. 41–1478). No peaks of SiO_2 and SiC can be found in the XRD patterns, which means that the undesirable side reactions of Si oxidation or reaction with carbon do not occur. To calculate the Si content of Si@FG/C, TG measurements were performed as

seen in Fig. 4b. For Si@FG/C-1, Si@FG/C-2and Si@FG/C-3, there are two weight loss processes in the temperature ranges of 400–500 ℃ and 500–800 ℃, which are attributed to the burning of amorphous carbon and FG, respectively. The slight weight gain at 800–900 ℃ can be ascribed to the minor oxidation of Si in air at high temperature. Thus, the residual mass after TG tests can be considered as the Si content in the composites,[33,37] that is about 8.0% for Si@FG/C-1, 11.0% for Si@FG/C-2 and 16.0% for Si@FG/C-3. As shown in Fig. 4c, the three Si-based composites have similar particle size distribution, which is 0–25 μm. Fig. 4d presents the Raman spectra of Si@FG/C, Si and FG. The peaks at 508 and 918 cm^{-1} are attributed to Si and the peaks at 1360 cm^{-1} and 1580 cm^{-1} are assigned to D-band and G-band of carbon materials and the value of I_D/I_G represents graphitization degree. The increased intensity ratio of I_D/I_G of Si@FG/C compared with FG suggests the formation of amorphous carbon from the pyrolysis of glucose and PVP.[38,39] To clarify the structure of pyrolytic carbon from the organic precursor, we carbonized glucose in 600 and 1000 ℃ for 4 h under Ar flow, and the obtained samples were characterization by XRD and Raman spectra (Fig. S1 in Supporting Information). Only broad peaks can be observed in the XRD patterns, indicating that the obtained carbon is in amorphous form. The results of Raman spectra also suggest that the pyrolytic carbon is amorphous. Usually, amorphous carbon has lower electrical conductivity than crystalline carbon. It is thus assumed that the amorphous carbon layer will compromise the intrinsic conductivity possessed by FG. To clarify this, EIS measurements were performed as seen in Fig. S2 of the Supporting Information. In the EIS plots, the intercept of the plots on the real axis represents the ohmic resistance of the battery components (electrode, electrolyte, etc.). We can see from the plots that although the introduction of amorphous carbon does increase the ohmic resistance, but the increase is not significant. In addition, the semicircles of the plots in the high-medium frequency region have a similar diameter, which means that the charge transfer resistance also shows no obvious change with the introduction of amorphous carbon. The results indicate that the amorphous carbon layer has not compromised the intrinsic conductivity possessed by FG.

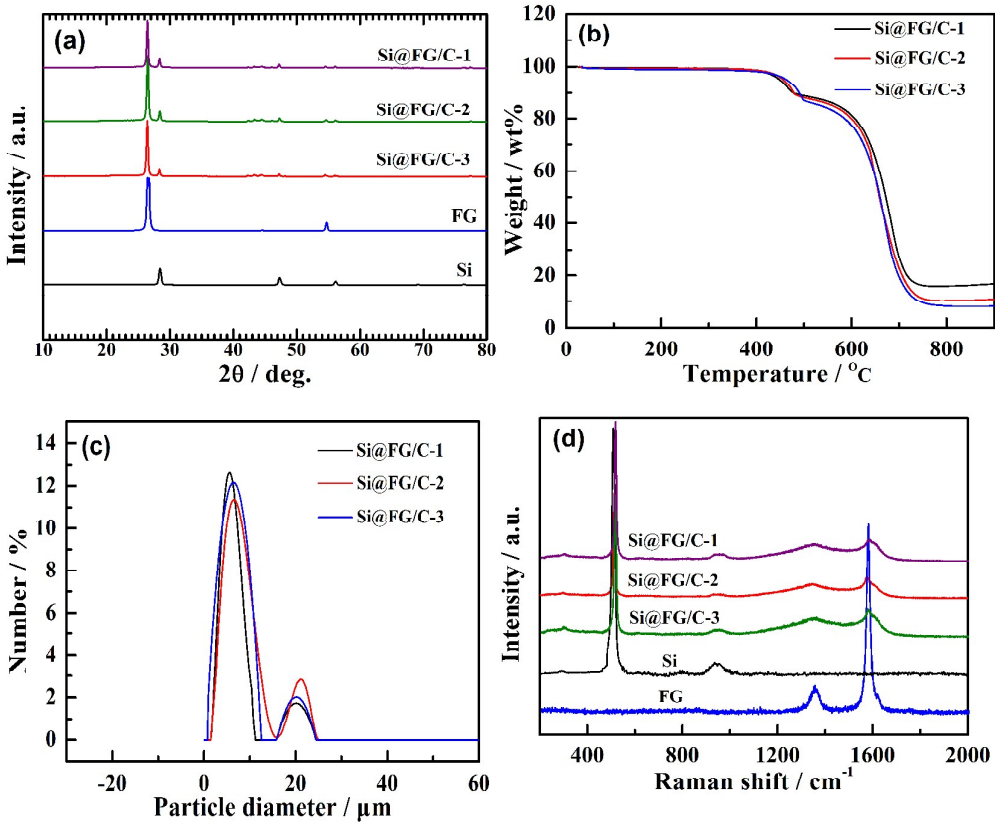

Fig. 4. (a) XRD patterns, (b) TG curves, (c) particle size distribution curves, and (d) Raman spectra of the as-received or prepared samples.

The electrochemical performance of samples was investigated by galvanostatic discharge-charge cycling at 0.2 A g^{-1} for the first five cycles and 0.5 A g^{-1} for later cycles. The effect of Si content on the battery performance was investigated in order to obtain an optimal composition of Si/FG@C composites aiming at long cycle life and high specific capacity. As shown in Fig. 5a, in the first discharge, the sloping curve is due to the organic electrolytes decomposition and the formation of SEI film. At the second and subsequent cycles, the surface of the electrode is stabilized by the SEI film, resulting stable cycling of the electrodes. Si/FG/C-1 presents a capacity of 587 mAh g^{-1} for the initial discharge, which is higher than the theoretical capacity of graphite. Since the amount of Si is only 8%, Si/FG/C-1 exhibits a lower initial capacity than Si. At the same time, amorphous carbon will lead to an increase of irreversible capacity. At higher Si contents of 11% and 16%, higher initial discharge capacities of 613 and 756 mAh g^{-1} can be achieved for

Si/FG/C-2 (Fig. 5c) and Si/FG/C-3 (Fig. 5e). To better understand the electrochemical reaction mechanism of the Si/FG/C composites, CV scanning was performed at 0.1 mV s^{-1}. As shown in Fig. 5b, in the first cycle, the broad cathodic peak between 0.8 and 1.2 V is generally linked to the decomposition of the organic electrolytes and the formation of SEI layer, since it is absent in the subsequent cycles.[40, 41] The cathodic peaks of below 0.2 V and the anodic peaks between 0.1 and 0.5 V were related to the lithiation/delithation reactions of FG, Si and amorphous carbon. In the subsequent cycles, there are three cathodic peaks ranging from 0 to 0.2 V, corresponding to the formation of Li_xC_6 and Li_xSi. For the oxidation process, the sharp peaks at approximately 0.2 V and small peaks at 0.25–0.45 V were related to the delithiation of Li_xC_6 and Li_xSi, respectively. Si/FG/C-2 (Fig. 5d) and Si/FG/C-3 (Fig. 5f) show the similar CV curves.

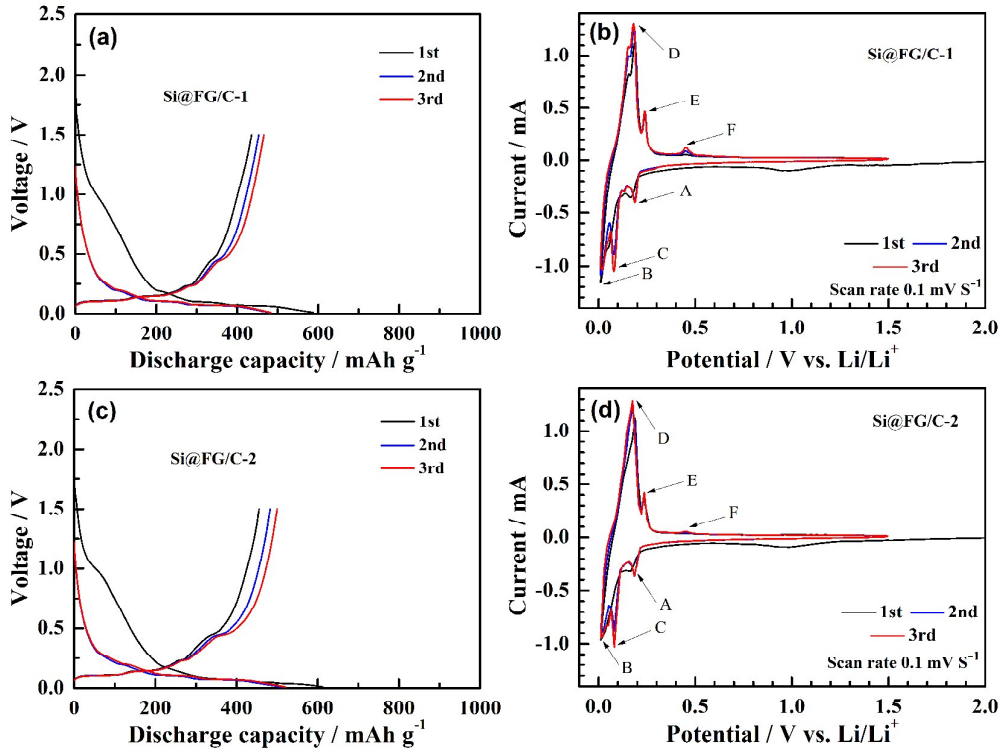

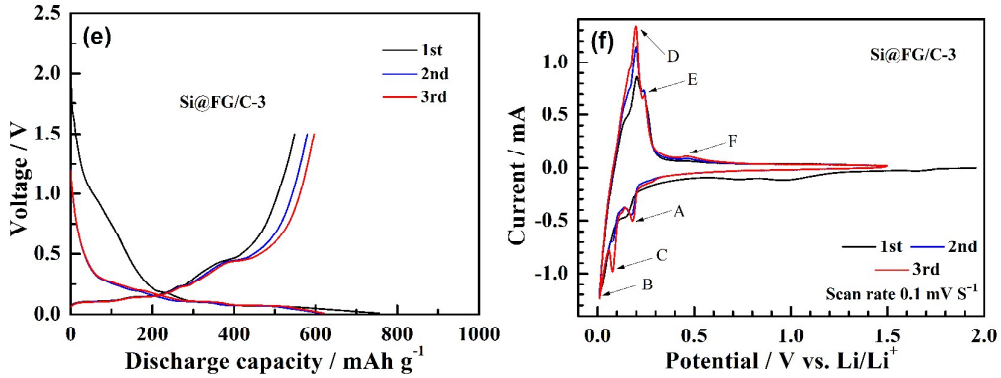

Fig 5. The first three discharge-charge curves at 0.2 A g^{-1} of (a) Si@FG/C-1, (c) Si@FG/C-2, and (e) Si@FG/C-3, and CV plots at 0.1 mV s^{-1} of (b) Si@FG/C-1, (d) Si@FG/C-2, and (f) Si@FG/C-3.

Fig. 6a shows the discharge capacity *vs.* cycle number of Si@FG/C microspheres. The initial discharge capacity of Si@FG/C-1was 587 mAh g^{-1} at a current density of 0.2 Ag^{-1} with a first columbic efficiency of 74%. From the 6th to 305th, the current density was increased to 0.5 Ag^{-1}. At this relatively high current density, a capacity over 420 mAh g^{-1} can be remained after 305 cycles, which is higher than the theoretical capacity of graphite. The capacity retention of this sample is 90% over 300 cycles, indicating good cycling stability, which can be ascribed to the buffering effect of free space in the porous Si@FG/C spheres. The amorphous carbon not only fixes the Si nanoparticles on the surface of graphite flakes but also absorbs the strain arising from the volume changes of Si particles upon cycling. In addition, the conductive networks constructed by FG and amorphous carbon also contribute to the good cycle life of the composite at high current density. The low initial columbic efficiency can be attributed to the presence of Si nanoparticles and amorphous carbon. Note that although increasing Si content can increase the initial discharge capacities of the composites, the cycle life is on the decrease, After 305 cycles, the capacities of Si@FG/C-2and Si@FG/C-3 decrease to 427 and 403 mAh g^{-1}, respectively. To clarify the respective contribution of the FG, amorphous carbon and Si to such properties as coulombic efficiency, discharge capacity, the electrochemical performance of Si, FG, amorphous was also investigated. As shown in Fig. S3 (Supporting Information), the discharge capacities of Si, FG and amorphous carbon are 2231, 360 and 686 mAh g^{-1} in the first cycle, and are around 10, 325 and 190

mAh g^{-1} after 100 cycles, and their initial coulombic efficiencies are 51%, 82% and 34%, respectively. It can be seen that the amorphous carbon has the lowest initial coulombic efficiency, Si has the highest initial capacity, and FG has the highest initial coulombic efficiency and the best cycling stability. Therefore, the ratio of Si, FG and amorphous carbon should be optimized to achieve optimized electrochemical performance. Fig. 6b shows the rate capability of Si@FG/C microspheres. Among the three composites, Si@FG/C-3 exhibits the best rate capability although it has the highest Si content. Even at a high current density of 5 A g^{-1}, the discharge capacity is still retained at about 200 mAh g^{-1}. To better understand the good cycling stability of Si@FG/C, ex situ SEM observation was conducted on Si@FG/C-1 (Fig. S4 in Supporting Information). It can be seen that the spherical structure still be kept after charge and discharge cycling due to buffering effect of free space in porous Si@FG/C-1 spheres for volume changes of Si and the fixing effect of amorphous carbon for Si particles on FG. In contrast, Si@FG (Fig. S5 in Supporting Information) shows rapid capacity fade in the initial cycles due to the lack of porous structure and fixing effect of amorphous carbon.

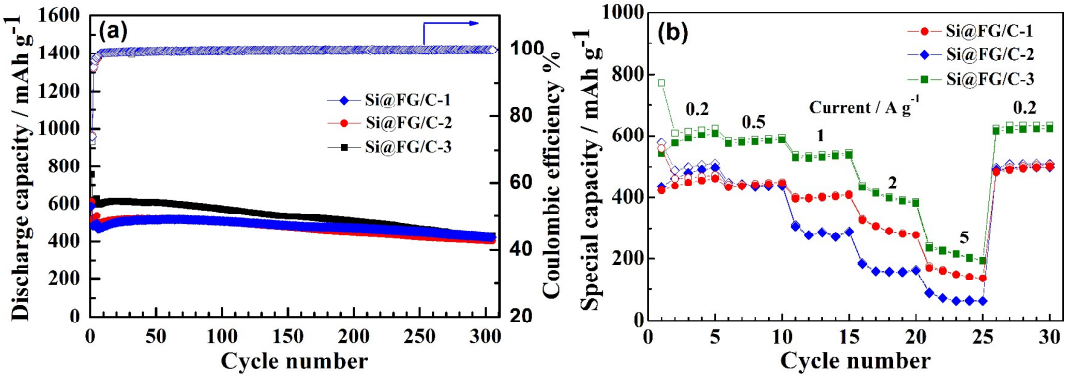

Fig.6. (a) Cycling stability and (b) rate capability of the Si@FG/C composites.

4. Conclusions

In conclusion, Si@FG/C porous microspheres for high-performance LIB anodes were successfully synthesized by ball-milling, spray drying and subsequent heat treatment. In this synthesis route, porous structure has formed in a single microsphere with Si nanoparticles uniformly dispersed. The

binding effect of glucose and PVP is responsible for the formation of the spherical structure. Such porous structure is critical for the excellent electrochemical performance because the porous structure offers free space for buffering the volume changes of Si during cycling. The amorphous carbon not only fixes the Si particles but also absorbs mechanical strain from the volume changes of Si. The conductive channels built by FG and amorphous carbon account for the good rate capability of the composites. Besides, the small size of Si particles is also favorable for good rate capability of the composites. As a result, the Si@FG/C composites show good cycle life and rate capability. The easy preparation and good electrochemical performance make Si@FG/C microspheres promising anodes for high-performance LIBs.

5. Acknowledgment

This work was supported by the National Basic Research Program of China (2013CB934001), the National Natural Science Foundation of China (No. 51572238), Zhejiang Provincial Natural Science Foundation of China under Grant No. LY15E010004, Key Science and Technology Innovation Team of Zhejiang Province under Grant Number 2010R50013, and Program for Innovative Research Team in University of Ministry of Education of China (IRT13037).

References

1 W.S. Kim, Y. Hwa, J.H. Shin, M. Yang, H.J. Sohn and S.H. Hong, *Nanoscale*, 2014, 6, 4297–4302.

2 B. Li, S.B. Yang, S.M. Li, B. Wang and J.H. Liu, *Adv.Energy Mater.*, 2015,5, 1500289.

3 N. Liu, H. Wu, M.T. McDowell, Y. Yao, C.M. Wang and Y. Cui, *Nano lett.*, 2012,12, 3315–3321.

4 M. Li, X.H. Hou, Y.J. Sha, J. Wang, S.J. Hu, X. Liu and Z.P. Shao, *J. Power Sources*, 2014,248,

721–728.

5 M.T. McDowell, S.W. Lee, W.D. Nix and Y. Cui, *Adv. Mater.*, 2013,25, 4966–4985.

6 H.P. Jia, P.F. Gao, J. Yang, J.L. Wang, Y.N. Nuli and Z. Yang, *Adv.Energy Mater.*, 2011,1, 1036–1039.

7 J. Park, G.P. Kim, I. Nam, S. Park and J. Yi, *Nanotechnology*, 2013, 24, 025602.

8 R.Y. Zhang, Y.J. Du, D. Li, D.K. Shen, J.P. Yang, Z.P. Guo, H.K. Liu, A.A. Elzatahry and D.Y. Zhao, *Adv. Mater.*, 2014,26, 6749–6755.

9 J. Xie, G.Q. Wang, Y. Huo, S.C. Zhang, G.S. Cao and X.B. Zhao,*Electrochim. Acta*, 2014, 135, 94–100.

10 N. Lin, Y. Han, L.B. Wang, J.B. Zhou,J. Zhou, Y.C. Zhu and Y.T. Qian,*Angew. Chem.Int. Edit.*, 2015,54, 3822–3825.

11 B. Wang, T.F. Qiu, X.L. Li, B. Luo, L. Hao, Y.B. Zhang and L.J. Zhi, *J. Mater. Chem. A*, 2015, 3, 494–498.

12 F.M. Hassan, R. Batmaz, J.D. Li, X.L. Wang, X.C. Xiao, A.P. Yu and Z.W. Chen, *Nat.Commun.*, 2015,6, 8597.

13 L. Pan, H.B. Wang, D.C. Gao, S.Y. Chen, L. Tan and L. Li, *Chem.Commun.*, 2014, 50, 5878–5880.

14 H. Wu, G.H. Yu, L.J. Pan, N.A. Liu, M.T. McDowell, Z.A. Bao and Y. Cui, *Nat Commun*, 2013, 4, 1943.

15 Z.D. Lu, N. Liu, H.W. Lee, J. Zhao, W.Y. Li, Y.Z. Li and Y. Cui, *ACS Nano*, 2015,9, 2540–2547.

16 F.S. Li, Y.S. Wu, J. Chou, M. Winter and N.L. Wu, *Adv. Mater.*, 2015,27, 130–137.

17 X. Su, Q.L. Wu, J.C. Li, X.C. Xiao, A. Lott, W.Q. Lu, B.W. Sheldon and J. Wu, *Adv. Energy*

Mater., 2014,4,1300882.

18 T. Bok, S. Choi, J. Lee and S. Park, *J. Mater. Chem. A*, 2014,2, 14195-14200.

19 Y. Yu, L. Gu, C.B. Zhu, S. Tsukimoto, P.A. van Aken and J. Maier, *Adv. Mater.*, 2010,22, 2247–2250.

20 B.R. Liu, P. Soares, C. Checkles, Y. Zhao and G.H. Yu, *Nano Lett.*, 2013,13, 3414–3419.

21 H. Wu, G. Chan, J.W. Choi, I. Ryu, Y. Yao, M.T. McDowell, S.W. Lee, A. Jackson, Y. Yang, L.B. Hu and Y. Cui, *Nat Nanotechnol*, 2012,7, 310–315.

22 L. Sun, T.T. Su, L. Xu and H.B. Du, *Phys. Chem. Chem. Phys.*, 2016,18, 1521–1525.

23 P.F. Gao, Y. Nuli, Y.S. He, J.Z. Wang, A.I. Minett, J. Yang and J. Chen, *Chem. Commun.*, 2010,46, 9149–9151.

24 J. Xie, G.Q. Wang, Y. Huo, S.C. Zhang, G.S. Cao and X.B. Zhao, *New J. Chem.*, 2014,38, 4177–4181.

25 S. Sim, P. Oh, S. Park and J. Cho, *Adv. Mater.*, 2013,25, 4498–4503.

26 H. Jiang, X. Zhou, G.G. Liu, Y.H. Zhou, H.Q. Ye, Y. Liu and K. Han, *Electrochim. Acta*, 2016,188, 777–784.

27 J.L. Yu, J. Yang, X.J. Feng, H. Jia, J.L. Wang and W. Lu, *Ind.Eng. Chem. Res.*, 2014,53, 12697–12704.

28 T.S.D. Kumari, D. Jeyakumar and T. P. Kumar, *RSC Adv.*, 2013,3, 15028–15034.

29 W. Wang, M. Tian, Y.J. Wei, S.-H. Lee, Y.-C. Lee and R.G. Yang, *Nano Energy*, 2013,2, 943–950.

30 J.Y. Liu, N. Li, M.D. Goodman, H.G. Zhang, E.S. Epstein, B. Huang, Z. Pan, J. Kim, J.H. Choi, X.J. Huang, J.H. Liu, K.J. Hsia, S.J. Dillon and P.V. Broun, *ACS Nano*, 2015,9, 1985–1994.

31 N. Liu, Z.D. Lu, J. Zhao, M.T. McDowell, H.W. Lee, W.T. Zhao and Y. Cui, *Nat Nanotechnol*,

2014,9, 187–192.

32 M.X. Gao, D.S. Wang, X.Q. Zhang, H.G. Pan, Y.F. Liu, C. Liang, C.X. Shang and Z.X. Guo, *J. Mater. Chem. A*, 2015,3, 10767–10776.

33 W.F. Ren, Z.L. Zhang, Y.H. Wang, Q.Q. Tan, Z.Y. Zhong and F.B. Su, *J. Mater. Chem. A*, 2015,3, 5859–5865.

34 D.S. Wang, M.X. Gao, H.G. Pan, Y.F. Liu, J.H. Wang, S.Q. Li and H.W. Ge, *J. Alloys Compd.*, 2014, 604, 130–136.

35 M.R. Su, Z.X. Wang, H.J. Guo, X.H. Li, S.L. Huang, W. Xiao and L. Gan, *Electrochim. Acta*, 2014,116, 230–236.

36 A. Paudel, Z.A. Worku, J. Meeus, S. Guns and G. Van den Mooter, *Int. J. Pharm.*, 2013,453, 253–284.

37 Z.L. Zhang, Y.H. Wang, W.F. Ren, Z.Y. Zhong and F.B. Su, *RSC Adv.*, 2014,4, 55010–55015.

38 T. Jawhari, A. Roid and J. Casado, *Carbon*, 1995,33, 1561–1565.

39 S. Gayathri, P. Jayabal, M. Kottaisamy and V. Ramakrishnan, *AIP Adv.*, 2014,4, 027116.

40 M.R. Su, Z.X. Wang, H.J. Guo, X.H. Li, S.L. Huang, L. Gan and W. Xiao, *Powder Technol.*, 2013,249, 105–109.

41 L.F. Cui, R. Ruffo, C.K. Chan, H.L. Peng and Y. Cui, *Nano Lett.*, 2009,9, 49.